

Flow Matching for Optimal Reaction Coordinates of Biomolecular System

Mingyuan Zhang,[†] Zhicheng Zhang,[‡] Yong Wang,^{*,†} and Hao Wu^{*,¶}

[†]*College of Life Sciences, Zhejiang University, Hangzhou 310027, China*

[‡]*School of Mathematical Sciences, Tongji University, Shanghai 200092, China*

[¶]*School of Mathematical Sciences, Institute of Natural Sciences, and MOE-LSC, Shanghai
Jiao Tong University, Shanghai 200240, China*

E-mail: yongwang_isb@zju.edu.cn; hwu81@sjtu.edu.cn

Abstract

We present Flow Matching for Reaction Coordinates (FMRC), a novel deep learning algorithm designed to identify optimal reaction coordinates (RC) in biomolecular reversible dynamics. FMRC is based on the mathematical principles of lumpability and decomposability, which we reformulate into a conditional probability framework for efficient data-driven optimization using deep generative models. While FMRC does not explicitly learn the well-established transfer operator or its eigenfunctions, it can effectively encode the dynamics of leading eigenfunctions of the system transfer operator into its low-dimensional RC space. We further quantitatively compare its performance with several state-of-the-art algorithms by evaluating the quality of Markov State Models (MSM) constructed in their respective RC spaces, demonstrating the superiority of FMRC in three increasingly complex biomolecular systems. Finally, we discuss its potential applications in downstream applications such as enhanced sampling methods and MSM construction.

1 Introduction

Reaction coordinate (RC) is the core object of biophysical studies using molecular dynamics (MD) simulation. On the one hand, with the technical advancement in computational hardware,¹ the MD trajectories of molecular systems with increasing length and complexity present a significant challenge for their biophysical interpretation due to their high dimensionality. By projecting these trajectories into a low-dimensional manifold parameterized by an RC, one can remarkably reduce the effort in understanding the underlying biophysical mechanism. For example, in the well-established Markov State Model (MSM) approach,² the dimension reduction of the raw trajectory data by optimal RCs is essential for the assignment of different conformations into the “microstates” which assume local equilibrium. On the other hand, many interesting biological phenomena at a timescale of seconds or even hours, are still out of the reach of current MD simulations. To accelerate MD simulation in such a scenario, enhanced sampling techniques, such as umbrella sampling³ or metadynamics,⁴ which biased the simulation along a given RC, are often utilized. However, in both scenarios, the efficacy of the strategy is strongly dependent on the “optimality” of the RC. Intuitively, optimal RC is a parameterization of a low-dimensional projection of the original system which encodes the full-dimensional system dynamics. To do so, the RC should distinguish between metastable states by assigning similar RC coordinates to kinetically close conformations. It should also accurately characterize the transition pathways and their associated transition states within limited dimensions.⁵ However, the determination of such RC, in general, cannot be accurately determined based on human expertise in increasingly complex biomolecular systems.

As a result, machine learning techniques have been gaining popularity in the determination of RC in a data-driven manner according to an optimization target, or loss function, based on a specific definition of RC in mathematical language. However, such a precise mathematical definition of optimal RC mutually agreed by the community has not yet been established.⁶⁻¹² The earliest attempts at such a definition are based on the splitting prob-

ability, also known as the committor function.^{13,14} Given two user-defined non-overlapping metastable states, labelled A and B (e.g. folded and unfolded state of a protein), the committor function $q_A(\mathbf{x}_0) := 1 - q_B(\mathbf{x}_0)$, which defined as the probability of reaching state A before state B given the starting conformation \mathbf{x}_0 , is argued as the optimal RC for the transition between A and B. Utilizing such definition, multiple machine learning algorithms^{10,11,15} have been proposed to compute optimal RC as the committor function with success in torsional isomerization, protein folding, and protein aggregation. However, a major problem of such a definition is that it relies on the human definition of states A and B, and sometimes such prior information might not be available or reliably provided.

Such an issue further motivates the development of unsupervised RC machine learning algorithms based on a loss function that can be purely computed from simulation data without any state labelling. One notable group of such unsupervised algorithms constructs the optimal RC under the mathematical framework provided by the variational approach to conformational dynamics (VAC)¹⁶ and its irreversible extension Variation Approach to the Markov Process (VAMP).¹⁷ Here, we focus solely on reversible dynamics fulfilling the detailed balance condition within the scope of VAC. Under the VAC viewpoint, the optimal RC is defined as the leading eigenfunctions of the system transfer operator (see Theory and Methods). Various VAC-based RC machine learning algorithms such as time-lagged independent component analysis (TICA)⁸ and its variants Koopman-reweighted TICA,¹⁸ kernel TICA,¹⁹ state reversible VAMPnets (SRV),⁷ etc. have been proposed to numerically approximate these eigenfunctions from data by seeking a linear combination of the basis function which maximizes autocorrelation. These algorithms have achieved great success in a wide range of biomolecular systems including protein folding,²⁰⁻²² protein-protein interaction,²³ ligand binding,^{24,25} etc., and have been widely accepted as a routine algorithm in the pipeline of Markov State Model (MSM) construction for their generality and robustness. Nevertheless, there are several pitfalls associated with such algorithms:^{12,26}

- The number of dimensions of the leading eigenfunctions can sometimes be redundant,

which makes them harder to interpret than the committor function and less applicable to enhanced sampling purposes.

- The accurate approximation of eigenfunctions is expensive since it requires extensive simulation data covering the whole conformational space.
- The linear regression nature of these algorithms may limit the expressivity of the learned RC.

To address these pitfalls, Bittracher et al.¹² have recently proposed a new theoretical framework for the unsupervised learning of optimal RC based on their previously developed transition manifold theory.^{26,27} Instead of approximating the leading eigenfunctions directly, they aimed to construct a low-dimensional RC space projected from the original full dimensional conformational space which preserves the major system dynamics described by the original system transfer operator. The parameterization of the basis functions of this projected space can then be viewed as the optimal RC. They further formulated mathematical definitions of such optimal RC, known as lumpability and decomposability. We found these formulations particularly attractive, as they have been theoretically well-established and numerically demonstrated on simple model systems that they can be computed in theory with less sampling required in comparison to the VAC-based algorithms. Furthermore, since these formulations only involve the modelling of original and projected transition probability, they are ideal optimization targets for deep generative modelling techniques with strong expressivity and robustness. However, they have not yet proposed or implemented a ready-to-use deep learning algorithm based on such formulations that can be directly applied to biomolecular MD trajectories. As a result, the efficacy of such formulations in computing RC for real-life biomolecular systems has not been investigated.

On the other hand, Tiwary et al.⁶ introduced an alternative perspective on optimal RC for unsupervised learning based on information theory.²⁸ They argued that an optimal RC should be a low-dimensional representation which preserves minimal information of the

system conformation at the current time step, while still being able to accurately predict the future system conformation after a short lag time. The predictability of such an RC is mathematically quantified by the mutual information between the current RC representation and the future full-dimensional conformation. Building on this concept, they developed an RC deep learning algorithm called the state predictive information bottleneck (SPIB),²⁹ which has been successfully applied to studying biophysical processes such as protein folding and membrane permeation of small molecules.³⁰ They also demonstrated the potential of their algorithm in improving other sampling or modelling techniques, such as enhanced sampling,³⁰ MSM construction,³¹ and the weighted ensemble method.³²

In this article, we 1) present a novel unsupervised deep learning algorithm for determining the optimal RC of biomolecular reversible dynamics, based on principles of lumpability and decomposability. We refer to this algorithm as Flow Matching for Reaction Coordinates (FMRC), following our recent mathematical analysis of the algorithm.³³ We then 2) perform a systematic comparison of the capability of learning optimal RC of different algorithms discussed above with FMRC.

For FMRC, we first reformulate the concepts of lumpability and decomposability to an equivalent conditional probability formulation that aligns with modern deep generative learning architectures. To further streamline the training process and improve modelling accuracy, we constructed our RC learning model as a continuous normalizing flow³⁴ conditioned (decoder) on a simple feed-forward neural network (encoder) which represents the optimal RC. We simplified the training process further by using a simulation-free training method as in flow matching.^{35,36} Such implementation leads to an easy-to-train, accurate RC deep learning algorithm with low variance, demonstrated across three increasingly complex protein folding systems, with minimal reliance on prior knowledge of the system.

We then evaluate the quality of the RCs generated by FMRC trained on these datasets by comparing them with those produced by a range of popular unsupervised algorithms. This evaluation is based on each algorithm’s ability to encode the major system dynamics

described by the original system transfer operator in their low-dimensional RC space. This is achieved by comparing the eigenvalues of the MSM constructed inside each RC space. To take account of the stochastic elements presented in these algorithms, we repeated the training process 10 times for each algorithm using consistent hyperparameters for each system, allowing us to assess the variance across different algorithms.

Our results demonstrate a significantly higher amount of dynamics preservation by the FMRC in the RC space than all other algorithms, along with a smaller training variance than all deep learning-based algorithms for all three systems. Moreover, for all three systems, we trained FMRC with a consistent training hyperparameters setting with only minor adjustments, demonstrating its robustness in training. Additionally, by tuning the lag time, we demonstrated that the free energy surface (FES) projected on the learned RC spaces can either preserve fine details or provide macroscopic interpretation for all three systems. Taken together, these results suggest FMRC is a promising tool for downstream applications such as enhanced sampling methods and MSM construction.

2 Theory and Methods

2.1 Transfer Operator

MD trajectories can be considered as a Markov process $\{\mathbf{x}_t\}$ which progressively evolves the configurational probability density $p_t(\mathbf{x})$ at time step t towards the system equilibrium distribution $\pi(\mathbf{x})$ in the state space Ω . This equilibrium distribution is unitary and corresponds to the Boltzmann distribution $\pi(\mathbf{x}) = Z^{-1} \exp(-\beta\mathcal{H}(\mathbf{x}))$, where Z is the partition function, \mathcal{H} is the system Hamiltonian and β is the inverse temperature $\beta = 1/(k_B T)$. Such Markov process has an associated transfer operator $\mathcal{T}(\tau)$, which propagates the weighted probability density at current time step t , $u_t(\mathbf{x}) = \pi(\mathbf{x})^{-1} p_t(\mathbf{x})$, to the weighted probability density after

a short lag time τ , $u_{t+\tau}(\mathbf{x}) = \pi(\mathbf{x})^{-1}p_{t+\tau}(\mathbf{x})$:

$$u_{t+\tau}(\mathbf{y}) = \mathcal{T}(\tau)u_t(\mathbf{y}) = \frac{1}{\pi(\mathbf{y})} \int_{\Omega} p_{\tau}(\mathbf{x}, \mathbf{y})\pi(\mathbf{x})u_t(\mathbf{x})d\mathbf{x} \quad (1)$$

where $p_{\tau}(\mathbf{x}, \mathbf{y})$ is the transition probability of a system conformation being \mathbf{x} at time t given that the system conformation being \mathbf{y} after a short lag time τ , which due to Markovianity, is only dependent on \mathbf{x} :

$$p_{\tau}(\mathbf{x}, \mathbf{y}) = \mathbb{P}(\mathbf{x}_{t+\tau} = \mathbf{y} \mid \mathbf{x}_t = \mathbf{x}) \quad (2)$$

Notice that in reversible dynamics considered in this article, p_{τ} satisfies the condition of detailed balance:

$$\pi(\mathbf{x})p_{\tau}(\mathbf{x}, \mathbf{y}) = \pi(\mathbf{y})p_{\tau}(\mathbf{y}, \mathbf{x}) \quad (3)$$

Under this condition, the transfer operator of a system is a self-adjoint operator and thus can undergo spectral decomposition that yields an infinite series of real eigenvalues λ_i and orthonormal eigenfunctions $\psi_i := \psi_i(\mathbf{x})$:

$$\mathcal{T}(\tau)\psi_i = \lambda_i\psi_i \quad (4)$$

where the eigenvalues λ_i are usually arranged in descending order, with the largest eigenvalue always being 1:

$$1 \equiv \lambda_0 > \lambda_1 > \lambda_2 > \dots > \lambda_{\infty} \quad (5)$$

The eigenvalues λ_i each corresponds to an implied timescale (ITS) t_i of the orthogonal process represented by its associated eigenfunction ψ_i :

$$t_i = -\frac{\tau}{\ln |\lambda_i|} \quad (6)$$

This indicates the first eigenfunction ψ_0 has an infinite timescale $t_0 \rightarrow \infty$. After evolving the dynamics by $\mathcal{T}(\tau)$ for a very long time, all the other eigenfunctions associated with an

eigenvalue $\lambda_i < 1$ will decay to zero, representing the system equilibrium:

$$\lim_{\tau \rightarrow \infty} \mathcal{T}(\tau)u_t(\mathbf{x}) = \psi_0 = 1 \quad (7)$$

The leading eigenfunctions from ψ_1 are therefore the slowest modes of the system corresponding to conformational transition processes between the metastable states of the system. From this viewpoint, if $\mathcal{T}(\tau)$ or ψ_i is available, one can trivially define the optimal RC as the leading eigenfunctions ψ_i of the system. However, neither $\mathcal{T}(\tau)$ nor ψ_i is analytically available for complex biomolecular systems. To tackle this issue, one well-established strategy is to utilize VAC to approximate $\mathcal{T}(\tau)$ or ψ_i in a data-driven manner (See Supporting Information).

2.2 Lumpability and Decomposability

While the VAC-based methods have been successfully applied to a wide range of biomolecular systems, as stated in the Introduction, computing RC using VAC-based algorithms has significant pitfalls. To address these issues, Bittracher et al.¹² proposed a set of novel mathematical definitions of optimal RC, known as lumpability and decomposability, following their earlier theoretical framework of transition manifold theory.^{26,27} Lumpability states that the optimal RC \mathbf{r}^{LD} should satisfy the following relationship for all time-lagged pairs $\{\mathbf{x}_t, \mathbf{x}_{t+\tau}\}$:

$$p_\tau(\mathbf{x}, \mathbf{y}) \approx \mathbb{P}(\mathbf{x}_{t+\tau} = \mathbf{y} \mid \mathbf{r}^{LD}(\mathbf{x}_t) = \mathbf{r}^{LD}(\mathbf{x})) \quad (8)$$

In words, if the RC is indeed optimal, the transition probability from conformation \mathbf{x} to conformation \mathbf{y} after a short lag time τ is only dependent on the low-dimensional RC values of the conformation $\mathbf{r}^{LD}(\mathbf{x})$, instead of its full-dimensional conformational coordinates \mathbf{x} . The name ‘‘lumpability’’ comes from that the optimal RC can effectively ‘‘lump’’ all kinetically close conformational coordinates together to a point in the RC space defined by $\mathbf{r}^{LD}(\mathbf{x})$.

In contrast, decomposability states that the optimal RC $\mathbf{r}^{LD}(\mathbf{x})$ should satisfy the fol-

lowing relationship for all time-lagged pairs $\{\mathbf{x}_t, \mathbf{x}_{t+\tau}\}$:

$$p_\tau(\mathbf{x}, \mathbf{y}) \approx \mathbb{P}(\mathbf{r}^{LD}(\mathbf{x}_{t+\tau}) = \mathbf{r}^{LD}(\mathbf{y}) \mid \mathbf{x}_t = \mathbf{x}) \cdot \pi_{local}(\mathbf{r}^{LD}(\mathbf{y}), \mathbf{y}) \quad (9)$$

where $\pi_{local}(\mathbf{r}, \mathbf{y})$ is the local equilibrium probability distribution of the conformation \mathbf{y} inside the set which shares the same value of $\mathbf{r}^{LD}(\mathbf{y}) = \mathbf{r}$. In words, this suggests that the transition from \mathbf{x} to \mathbf{y} can be “decomposed” into a two-step process:

1. The transition from \mathbf{x} to any conformation that belongs to the level set $\{\mathbf{y}' \mid \mathbf{y}' \in \Omega, \mathbf{r}^{LD}(\mathbf{y}') = \mathbf{r}^{LD}(\mathbf{y})\}$.
2. The local equilibration to the conformation \mathbf{y} inside this level set.

Remark 1. *Here we define decomposability in a manner that slightly deviates from the formalism presented by Bittracher et al.¹² It can be proved that the two definitions are indeed equivalent (see³³). We choose the current formulation for its ease of understanding.*

Furthermore, in reversible dynamics satisfying equation 3, these two conditions have been shown to be equivalent.¹² Notice although equation 8 and equation 9 do not involve modelling ψ_i or $\mathcal{T}(\tau)$ explicitly, the modelling of transition probability $p_\tau(\mathbf{x}, \mathbf{y})$ is closely linked to the transfer operator theory since $\mathcal{T}(\tau)$ is dependent on $p_\tau(\mathbf{x}, \mathbf{y})$ as in equation 1. In fact, if we consider the projected dynamics $\{\mathbf{r}_t^{LD}\}$ inside the \mathbf{r}^{LD} space, which is equivalently governed by a reduced transfer operator $\mathcal{T}_r(\tau)$ in the RC space, it can be shown that $\mathcal{T}_r(\tau)$ is a close approximation to the original system $\mathcal{T}(\tau)$.²⁷ As a result, the leading eigenvalues λ_i^r and eigenfunctions ψ_i^r of $\mathcal{T}_r(\tau)$ are also close approximations to the original leading λ_i and ψ_i . Physically, this means the full-dimensional systems dynamics, in terms of the major slow modes (ψ_i) and their associated timescales (λ_i), are encoded in the RC space with a minimum loss, if the RC is indeed optimal.

2.3 Flow Matching for Reaction Coordinates (FMRC)

2.3.1 Modelling Objectives

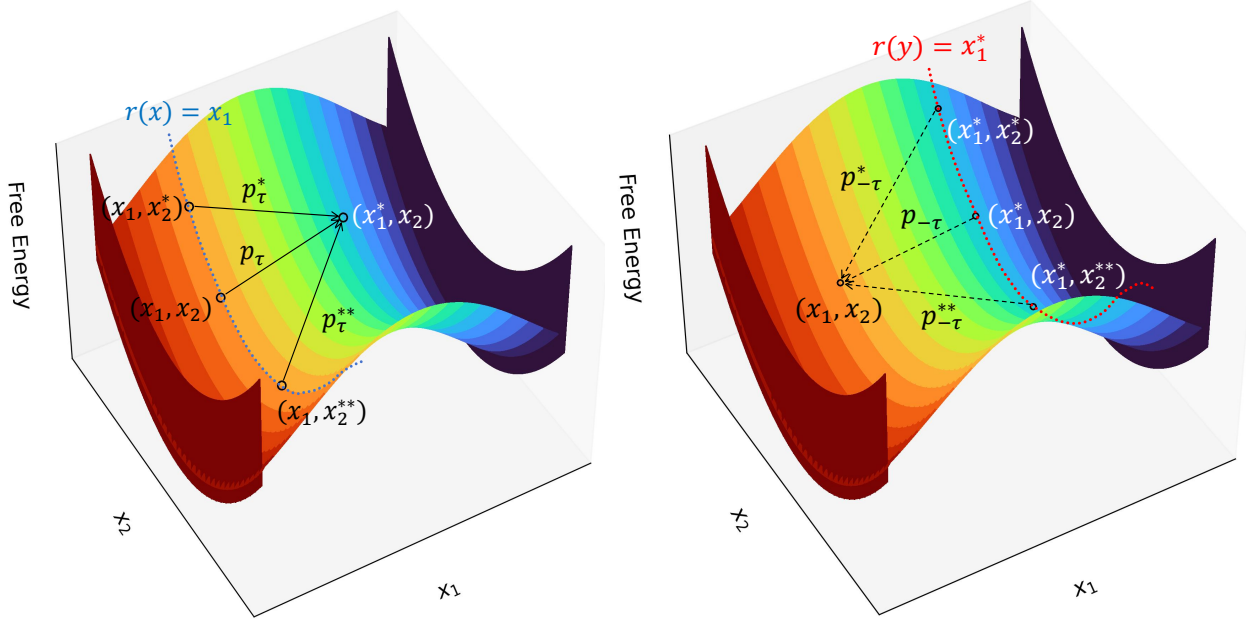


Figure 1: 4D plots of an optimal RC that satisfies both lumpability (left) and decomposability (right) for a 2D model system. The x -axis and y -axis of the plot are the 2D coordinates of the system. The z -axis represents the relative free energy of each coordinate. The color bar represents the value of an optimal RC $\mathbf{r} = x_1$. The initial coordinate \mathbf{x}_t of a transition with lag time τ is denoted in black and the final coordinate $\mathbf{x}_{t+\tau}$ is denoted in white. (left) An $\mathbf{r}(\mathbf{x})$ isoline of the initial coordinates is shown as a blue dotted line. We further denote three initial coordinates on this isoline as $\mathbf{x}^* := (x_1, x_2^*)$, $\mathbf{x} := (x_1, x_2)$ and $\mathbf{x}^{**} := (x_1, x_2^{**})$. Three Markovian transitions from these coordinates to a final coordinate (x_1^*, x_2) are shown as black arrows and the probabilities of these transitions are denoted as $p_\tau^* := p_\tau(\mathbf{x}^*, \mathbf{y})$, $p_\tau := p_\tau(\mathbf{x}, \mathbf{y})$ and $p_\tau^{**} := p_\tau(\mathbf{x}^{**}, \mathbf{y})$ depending on their initial x_2 values. (right) An $\mathbf{r}(\mathbf{y})$ isoline of the final coordinates is shown as a red dotted line. We further denote three final coordinates on this isoline as $\mathbf{y}^* := (x_1^*, x_2^*)$, $\mathbf{y} := (x_1^*, x_2)$ and $\mathbf{y}^{**} := (x_1^*, x_2^{**})$. Three Markovian transitions from the initial coordinate (x_1, x_2) to these coordinates are shown as backward black dotted arrows to emphasize that this is not a backward transition but the backward transition probability defined in equation 10. The probabilities of these transitions are denoted as $p_{-\tau}^* := p_{-\tau}(\mathbf{y}^*, \mathbf{x})$, $p_{-\tau} := p_{-\tau}(\mathbf{y}, \mathbf{x})$ and $p_{-\tau}^{**} := p_{-\tau}(\mathbf{y}^{**}, \mathbf{x})$ depending on their final x_2 values.

We next move on to present our novel algorithm, FMRC, for the computation of optimal RC as $\mathbf{r}^{FMRC} \approx \mathbf{r}^{LD}$ based on lumpability and decomposability. For the ease of analysis, we

introduce the backward transition probability

$$p_{-\tau}(\mathbf{y}, \mathbf{x}) = \mathbb{P}(\mathbf{x}_t = \mathbf{x} \mid \mathbf{x}_{t+\tau} = \mathbf{y}) \quad (10)$$

which represents the posterior distribution of the state \mathbf{x}_t given the future state $\mathbf{x}_{t+\tau}$. Then the conditions of lumpability and decomposability (Equations 8 and 9) can be both expressed in terms of conditional probabilities for all time-lagged pairs $\{\mathbf{x}_t, \mathbf{x}_{t+\tau}\}$:

$$\text{Lumpability} \rightarrow p_{\tau}(\mathbf{x}, \mathbf{y}) \approx \mathbb{P}(\mathbf{x}_{t+\tau} = \mathbf{y} \mid \mathbf{r}^{LD}(\mathbf{x}_t) = \mathbf{r}^{LD}(\mathbf{x})) \quad (11A)$$

$$\text{Decomposability} \rightarrow p_{-\tau}(\mathbf{y}, \mathbf{x}) \approx \mathbb{P}(\mathbf{x}_t = \mathbf{x} \mid \mathbf{r}^{LD}(\mathbf{x}_{t+\tau}) = \mathbf{r}^{LD}(\mathbf{y})) \quad (11B)$$

The proof of equation 11B can be found in the work of Zhang et al.³³ To provide a physically intuitive interpretation of equations 11A and 11B, we use a simple 2D double well potential to illustrate this idea (Figure 1). It is not difficult to see for this simple system, the x-axis coordinate, x_1 , is the only relevant degree to the transition process, and therefore, an intuitive optimal RC could be $\mathbf{r} = x_1$. In Figure 1 (left), three Markovian transitions are initiated on the same $\mathbf{r}(\mathbf{x}) = x_1$ isoline and our lumpability formulation from equation 10A states that $p_{\tau}^* = p_{\tau} = p_{\tau}^{**}$ (See Figure 1 legend for their definition). This is reasonable, since the fluctuation along the x_2 coordinate does not involve crossing any energy barriers and therefore, should be very fast. The actual transition-limiting degree is x_1 and should be the major contributor to p_{τ}^* , p_{τ} or p_{τ}^{**} . Thus, the probability of any transition initiates from the blue isoline to \mathbf{y} should be a close approximation to $p_{\tau}(\mathbf{x}, \mathbf{y})$ in this case. The same logic follows for our decomposability formulation. The fluctuation along the x_2 coordinate is expected to be very fast and should not affect $p_{-\tau}^*$, $p_{-\tau}$ or $p_{-\tau}^{**}$ significantly. As a result, as our decomposability formulation stated, given that the final coordinates residing on the red isoline, the probability of finding the initial coordinate at \mathbf{x} does not depend on the exact location of the final coordinate on the isoline.

Therefore, if we would like to approximate \mathbf{r}^{LD} as \mathbf{r}^{FMRC} in a data-driven manner, we can minimize the difference between the left hand side (l.h.s) and the right hand side (r.h.s.) of equations 11A and 11B for all time-lagged pairs $\{\mathbf{x}_t, \mathbf{x}_{t+\tau}\}$ by inserting \mathbf{r}^{FMRC} as \mathbf{r}^{LD} . Assuming sufficient sampling, the l.h.s. of both equations could be trivially represented as the empirical distribution from the MD trajectory dataset. On the other hand, we model the r.h.s of both equations together with the optimal RC \mathbf{r}^{FMRC} in our FMRC algorithm, which is detailed below. The graphical representations of our algorithms are depicted in Figure 2.

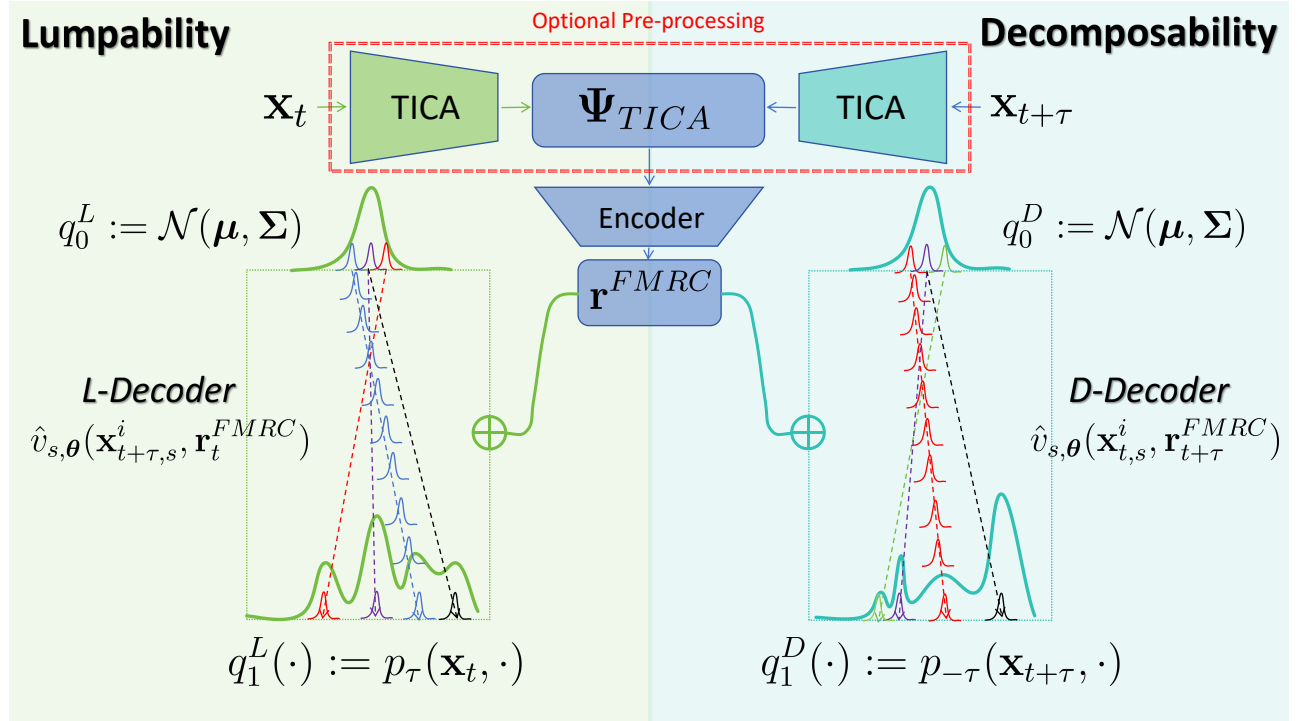


Figure 2: The overall architecture of FMRC. For each time-lagged pair $\{\mathbf{x}, \mathbf{x}_t\}$, they are pre-processed by TICA (optional) and encoded by the encoder. The L-decoder or D-decoder then optimizes the vector field $\hat{v}_{s,\theta}(\mathbf{x}_{t+\tau,s}^i, \mathbf{r}_t^{FMRC})$ or $\hat{v}_{s,\theta}(\mathbf{x}_{t,s}^i, \mathbf{r}_{t+\tau}^{FMRC})$ conditioned on (denoted as \oplus) the latent variable $\mathbf{r}^{FMRC}(\mathbf{x}_t)$ or $\mathbf{r}^{FMRC}(\mathbf{x}_{t+\tau})$ of the linear interpolation Gaussian path which transforms independent samples in q_0^L or q_0^D into independent samples in q_1^L or q_1^D , respectively. Please refer to the main text for a detailed explanation.

2.3.2 Representing \mathbf{r}^{LD} as an encoder

We construct our \mathbf{r}^{FMRC} in a two-step process:

1. (Optional) Compute a TICA transformation $\Psi_{TICA} = [\psi_1, \psi_2, \dots, \psi_{d_{int}}]^\top$ at the training

lag time τ with the trajectory data and truncate the series at an intermediate number of dimensions d_{int} . This is not strictly necessary but we found this option is the simplest and the most physically intuitive way for easier and better \mathbf{r}^{FMRC} learning for biomolecular systems we tested in this article, especially for more complex systems. Thus, all FMRC models in this article are trained with this pre-processing step. We will discuss the choice of d_{int} below.

2. Apply a neural network transformation $\Xi_{nn,\theta}^{Encoder}$, which we refer to as the encoder, to Ψ_{TICA} (or directly to \mathbf{x}) to yield a low-dimensional latent variable as \mathbf{r}^{FMRC} :

$$\mathbf{r}^{FMRC} = \Xi_{nn,\theta}^{Encoder}(\Psi_{TICA}) \quad (12)$$

2.3.3 Flow Matching

With \mathbf{r}^{FMRC} at hand, we proceed to model $\mathbb{P}(\mathbf{x}_{t+\tau} = \mathbf{y} \mid \mathbf{r}^{FMRC}(\mathbf{x}_t) = \mathbf{r}^{FMRC}(\mathbf{x}))$ and $\mathbb{P}(\mathbf{x}_t = \mathbf{x} \mid \mathbf{r}^{FMRC}(\mathbf{x}_{t+\tau}) = \mathbf{r}^{FMRC}(\mathbf{y}))$ using continuous normalizing flow (CNF).³⁴ CNF is a generative modelling technique which allows the parameterization of a complex target probability distribution $q_1 := q_1(\mathbf{z})$ of a random variable \mathbf{z} from a simple prior probability distribution $q_0 := q_0(\mathbf{z})$ that allows efficient sampling. This is achieved by a process which propagates the prior distribution q_0 , through a mixture of paths $q_s := q_s(\mathbf{z})$, towards the target probability q_1 that is governed by an ordinary differential equation (ODE). Specifically, we use a novel simulation-free CNF training method, known as flow matching (FM),³⁵ for our training process. In FM, instead of running the ODE simulation explicitly, we use a time-dependent vector field v_s to model the probability path q_s governed by the ODE implicitly

$$\frac{d\mathbf{z}_s}{ds} = v_s(\mathbf{z}_s) \quad (13)$$

where $\mathbf{z}_0 \sim q_0$ and s is a scalar ranging between 0 and 1 which can be interpreted as the ‘‘time’’ of the propagation process. To distinguish it from the system’s physical time t , we will

denote the virtual time in flow matching by s throughout the following discussion.

Interestingly, since v_s does not make any assumption on the path mixture q_s of the propagation,^{35,36} we can specify an arbitrary propagation path as q_s . Here, we follow the basic form of FM,³⁶ which specifies q_s in a way that individual samples $\mathbf{z}_0^i, \mathbf{z}_1^i$ from q_0 and q_1 are independently linearly interpolated via a Gaussian path. Under this setting, given that $\mathbf{z}_0^i, \mathbf{z}_1^i$ are the end points of the linear interpolation, \mathbf{z}_s^i on this interpolation can be sampled as:

$$\mathbf{z}_s^i \sim p_s(\mathbf{z}_s^i | \mathbf{z}_0^i, \mathbf{z}_1^i) = \mathcal{N}(\boldsymbol{\mu}_s, \boldsymbol{\sigma}) \quad (14)$$

where $\mathcal{N}(\boldsymbol{\mu}_s, \boldsymbol{\sigma})$ is a Gaussian with mean $\boldsymbol{\mu}_s = s\mathbf{z}_1^i + (1-s)\mathbf{z}_0^i$ and diagonal covariances $\boldsymbol{\sigma}$ with all entries as a small value. The value of the vector field along this specific interpolation path is:

$$v_s(\mathbf{z}_s^i | \mathbf{z}_0^i, \mathbf{z}_1^i) = \mathbf{z}_1^i - \mathbf{z}_0^i \quad (15)$$

Tong et al.³⁶ further show that under such setting, we can parameterize the vector field $\hat{v}_{s,\boldsymbol{\theta}}$ for the propagation by minimizing the following loss function \mathcal{L}_{FM} , which is an expectation over all individual samples $\mathbf{z}_0^i, \mathbf{z}_1^i$ from q_0 and q_1 :

$$\mathcal{L}_{FM}(\boldsymbol{\theta}) = \mathbb{E}[\|\hat{v}_{s,\boldsymbol{\theta}}(\mathbf{z}_s^i) - (\mathbf{z}_1^i - \mathbf{z}_0^i)\|^2] \quad (16)$$

where s is sampled uniformly between the interval $[0, 1]$. In the case where \mathcal{L}_{FM} is ideally minimized, the ODE defined by Equation 13 can accurately transform samples from the distribution q_0 into the distribution q_1 .

Remark 2. *More rigorously, if $\boldsymbol{\sigma} > \mathbf{0}$ in equation 14, the distributions governed by the ODE obtained from FM at $s = 0$ and $s = 1$ are given by $q_0 * \mathcal{N}(\mathbf{0}, \boldsymbol{\sigma})$ and $q_1 * \mathcal{N}(\mathbf{0}, \boldsymbol{\sigma})$, respectively, where $*$ denotes the convolution operator for probability density functions. As $\boldsymbol{\sigma} \rightarrow \mathbf{0}$, these distributions converge to q_0 and q_1 . In our experiments, we choose a small but positive $\boldsymbol{\sigma}$, primarily to ensure numerical stability during training.*

2.3.4 Flow Matching as Decoders

In FMRC, we define q_0 and q_1 separately for modeling lumpability and decomposability in parallel, which we denoted as q_0^L, q_0^D, q_1^L and q_1^D , respectively. We first define the prior distribution, q_0^L and q_0^D , as:

$$q_0^L = q_0^D := \mathcal{N}(\boldsymbol{\mu}, \boldsymbol{\Sigma}) \quad (17)$$

where $\mathcal{N}(\boldsymbol{\mu}, \boldsymbol{\Sigma})$ is a Gaussian distribution with mean and diagonal covariance being the mean and variance of $\boldsymbol{\Psi}_{TICA}$: $\boldsymbol{\mu} = [\mu(\psi_1^{TICA}), \dots, \mu(\psi_{d_{int}}^{TICA})]^\top$ and $\boldsymbol{\Sigma} = \text{diag}[\sigma^2(\psi_1^{TICA}), \dots, \sigma^2(\psi_{d_{int}}^{TICA})]$. We then define the target distribution, q_1^L and q_1^D as:

$$q_1^L(\cdot) := p_\tau(\mathbf{x}_t, \cdot) \quad (18A)$$

$$q_1^D(\cdot) := p_{-\tau}(\mathbf{x}_{t+\tau}, \cdot) \quad (18B)$$

for given \mathbf{x}_t and $\mathbf{x}_{t+\tau}$. Following the FM training objective from equation 16, we can parameterize q_1^L and q_1^D by regressing the vector fields $\hat{v}_{s,\boldsymbol{\theta}}(\mathbf{x}_{t+\tau,s}^i, \mathbf{x}_t)$ and $\hat{v}_{s,\boldsymbol{\theta}}(\mathbf{x}_{t,s}^i, \mathbf{x}_{t+\tau})$ through minimizing the loss functions \mathcal{L}^L and \mathcal{L}^D :

$$\mathcal{L}^L(\boldsymbol{\theta}) = \mathbb{E}[|\hat{v}_{s,\boldsymbol{\theta}}(\mathbf{x}_{t+\tau,s}^i, \mathbf{x}_t) - (\mathbf{x}_{t+\tau} - \mathbf{x}_{t+\tau,0}^i)|^2] \quad (19A)$$

$$\mathcal{L}^D(\boldsymbol{\theta}) = \mathbb{E}[|\hat{v}_{s,\boldsymbol{\theta}}(\mathbf{x}_{t,s}^i, \mathbf{x}_{t+\tau}) - (\mathbf{x}_t - \mathbf{x}_{t,0}^i)|^2] \quad (19B)$$

Similar to equation 15, $\mathbf{x}_{t+\tau,s}^i$ or $\mathbf{x}_{t,s}^i$ denotes samples from the Gaussian path at “time” s through equation 13. $\mathbf{x}_{t+\tau}, \mathbf{x}_t$ are individual samples from the target distribution q_1^L, q_1^D (hence directly from the trajectory dataset) and $\mathbf{x}_{t+\tau,0}^i, \mathbf{x}_{t,0}^i$ are individual samples from prior distribution q_0^L, q_0^D . Similarly, s is uniformly sampled between 0 and 1. Notice that in order to model the conditional probability $p_\tau(\mathbf{x}_t, \cdot)$ and $p_{-\tau}(\mathbf{x}_{t+\tau}, \cdot)$, we let the vector fields $\hat{v}_{s,\boldsymbol{\theta}}(\mathbf{x}_{t+\tau,s}^i, \mathbf{x}_t)$ and $\hat{v}_{s,\boldsymbol{\theta}}(\mathbf{x}_{t,0}^i, \mathbf{x}_{t+\tau})$ condition on \mathbf{x}_t and $\mathbf{x}_{t+\tau}$ as well, in contrast to the original FM training objective from equation 16. Furthermore, if we consider conditioning

on the latent variables of the encoder $\mathbf{r}_t^{FMRC} := \mathbf{r}^{FMRC}(\mathbf{x}_t)$ and $\mathbf{r}_{t+\tau}^{FMRC} := \mathbf{r}^{FMRC}(\mathbf{x}_{t+\tau})$ and minimize the following loss functions instead:

$$\tilde{\mathcal{L}}^L(\boldsymbol{\theta}) = \mathbb{E}[\|\hat{v}_{s,\boldsymbol{\theta}}(\mathbf{x}_{t+\tau,s}^i, \mathbf{r}_t^{FMRC}) - (\mathbf{x}_{t+\tau} - \mathbf{x}_{t+\tau,0}^i)\|^2] \quad (20A)$$

$$\tilde{\mathcal{L}}^D(\boldsymbol{\theta}) = \mathbb{E}[\|\hat{v}_{s,\boldsymbol{\theta}}(\mathbf{x}_{t,0}^i, \mathbf{r}_{t+\tau}^{FMRC}) - (\mathbf{x}_t - \mathbf{x}_{t,0}^i)\|^2] \quad (20B)$$

It can be seen that the minimum of equations 20A and 20B provides an upper bound of 19A and 19B and they are equal if and only if \mathbf{r}^{FMRC} satisfies lumpability and decomposability stated in equations 11A and 11B.³³ Thus, for FMRC, we assemble the encoder with both decoders and minimize the FMRC loss function $\mathcal{L}^{FMRC}(\boldsymbol{\theta})$ as

$$\mathcal{L}^{FMRC}(\boldsymbol{\theta}) = \tilde{\mathcal{L}}^L(\boldsymbol{\theta}) + \tilde{\mathcal{L}}^D(\boldsymbol{\theta}) \quad (21)$$

to optimize all parameters $\boldsymbol{\theta}$ simultaneously with back propagation. Once equation 21 is properly minimized, \mathbf{r}^{FMRC} will satisfy lumpability and decomposability and hence $\mathbf{r}^{FMRC} \approx \mathbf{r}^{LD}$.

2.4 The Comparison of RC Learning Algorithms

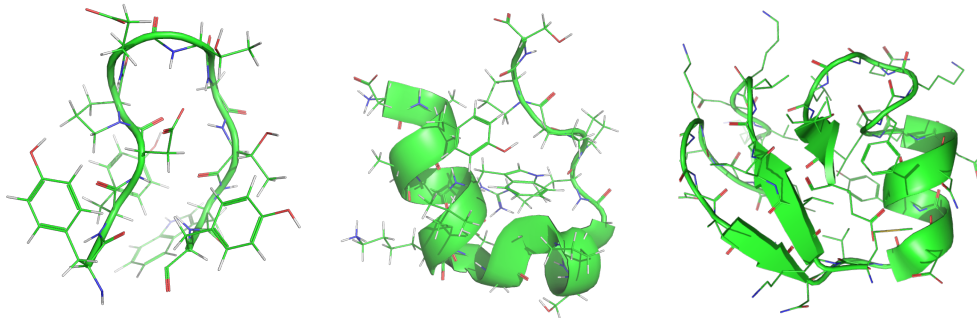


Figure 3: Extensively sampled trajectories of three biomolecular systems used for FMRC performance evaluation and RC comparison in this study: (left) chignolin variant CLN025 (PDB ID: 2RVD), (middle) Trp-Cage (PDB ID: 2JOF) and (right) NTL-9 (PDB ID: 2HBA).

To further test the efficacy of FMRC, we compared the optimality of \mathbf{r}^{FMRC} with RC learned by TICA⁸ (denoted as \mathbf{r}^{TICA}), SRV⁷ (denoted as \mathbf{r}^{SRV}) and SPIB²⁹ (denoted as \mathbf{r}^{SPIB}) using the same dataset. Detailed descriptions of these algorithms are provided in the Supporting Information. To ensure a fair quantitative evaluation of RC optimality, we adopted a simple strategy based on VAC¹⁶ and MSM² (see Supporting Information). We use three extensively sampled (~ 0.1 - 1.1 ms) MD trajectory datasets of mini-protein folding with increased complexity, which involves the formation of a range of secondary structures such as beta-hairpins or alpha helices from D. E. Shaw research³⁷ (Figure 3). This data-rich scenario was assumed to maximize the performance of all methods, leaving the investigation of sampling efficiency for RC learning to future studies. We then learned \mathbf{r}^{TICA} , \mathbf{r}^{SRV} , \mathbf{r}^{FMRC} and \mathbf{r}^{SPIB} from the same datasets using the same τ and performed k-means clustering in these RC spaces using an equal number of clusters. For \mathbf{r}^{FMRC} and \mathbf{r}^{SPIB} , each dimension of the RC is normalized between 0 and 1 before clustering, whereas for \mathbf{r}^{TICA} and \mathbf{r}^{SRV} , the eigenvectors were scaled to represent a kinetic distance³⁸ for optimal clustering. Finally, we constructed MSMs using cluster assignments from the different RC spaces with the same τ_{MSM} to ensure high-quality MSMs that obey Markovianity.

To assess and compare the optimality of different RCs, we evaluated the eigenvalues $\hat{\lambda}_i^{MSM}$ of the leading eigenvectors $\hat{\psi}_i^{MSM}$ from the MSMs constructed in each RC space. Given that the same hyperparameters (see Supporting Information) were used throughout the construction process and assuming minimal performance differences in the k-means algorithm across all RC spaces, we inferred the quality of the original RCs implicitly from the quality of the constructed MSMs based on VAC: the higher the eigenvalues λ_i^{MSM} , the higher the dynamical content preserved in the RC space and the better the RC. The same strategy was also employed to determine the optimal truncation dimension d_{int} for Ψ_{TICA} during FMRC pre-processing for all systems in this study.

Notice that we do not intend to restrict the scope of the FMRC algorithm or its comparison solely to MSM construction. Instead, we aim to explore broader potential downstream

applications such as enhanced sampling methods. In common enhanced sampling techniques such as umbrella sampling or metadynamics, the RC used to apply bias potential is typically limited a small number of dimensions (usually 2) for algorithmic efficiency. Therefore, we constrained the dimensionality of the RC to 2 across all learning algorithms. This also facilitates easier visualization and hence better human interpretation of the system dynamics.

Moreover, the hyperparameter τ plays an essential role in filtering out fast dynamics with timescales t_i below this threshold. For enhanced sampling purposes, the ideal RC should capture as many slow processes as possible. To achieve this, we used a relatively small τ across all algorithms for RC comparison. Nevertheless, we also performed a comparison of \mathbf{r}^{FMRC} learned with different τ to examine the impact of this hyperparameter on RC learning by FMRC.

Another important aspect in the evaluation of the RC machine learning algorithm is the variance of performance by these algorithms due to stochasticity from e.g. random seeds. In practical applications, it would be tedious and inefficient to repeat learning with the same hyperparameters and different random seeds for better performance. Therefore, after tuning the hyperparameters for satisfactory learning performance, we repeatedly learn 10 RCs using the same hyperparameters for each algorithm in each example. We then compare the mean and standard deviation of the eigenvalues $\hat{\lambda}_i^{MSM}$ to incorporate algorithm consistency into our comparison.

Finally, to investigate the origin of the differences in the RC learning performance between different algorithms, we projected all trajectory data points to different RC spaces and performed a PCCA+³⁹ analysis to investigate the ability to distinguish different metastable states in the RC spaces learned by different algorithms.

2.5 Hyperparameters and Software Packages

Another notable feature of the FMRC algorithm is that FMRC is very easy to train following our training protocol. For all three systems, we used the same feature selection strategy,

only adjusted d_{int} and τ and left hyperparameters such as learning rate, number of hidden layers/hidden nodes, and training epochs invariant for all three examples to achieve good performance. This should be pretty useful in practical applications since d_{int} and τ are more physically intuitive than tuning the size or learning rate of the neural networks. For \mathbf{r}^{SRV} and \mathbf{r}^{SPIB} , instead of running an exhaustive search for optimal training hyperparameters, we reference to the training protocols in previous studies^{21,31} utilizing these algorithms for similar systems and apply the same set of hyperparameters for all three examples. See Supporting Information for a detailed description of feature selection and model training for \mathbf{r}^{TICA} , \mathbf{r}^{SRV} , \mathbf{r}^{FMRC} and \mathbf{r}^{SPIB} together with subsequent MSM construction in these spaces.

We performed TICA, k-means clustering, MSM construction and PCCA+ using the Deeptime⁴⁰ library. All neural network models were trained with PyTorch 2.2.2 with CUDA support. We trained SRV using the code from: <https://github.com/andrewlferguson/snrv> and trained SPIB using the code from: <https://github.com/wangededi1997/spib>. The code of FMRC is available at: https://github.com/Mingyuan00/Flow_Matching_for_RC and we have uploaded all our analysis scripts and PyTorch model .pt files to Zenodo at <https://zenodo.org/records/13474614>.

3 Results and Discussion

3.1 FMRC Application to Chignolin Variant CLN025

We first demonstrate the efficacy of our FMRC algorithm using a 106 μ s trajectory of a mini-protein chignolin variant CLN025 (YYDPETGTWY, 10 amino acids, PDB ID: 2RVD) simulated at 340K. In solution, CLN025 maintains a stable beta-hairpin structure under room temperature and can interconvert between this hairpin structure (“folded”) with a fully extended conformation (“unfolded”) at its melting temperature of approximately 340K. The three-dimensional atomic coordinates were first converted into an extensive set of internal coordinates including interatomic distances and torsional angles (see Supporting Information

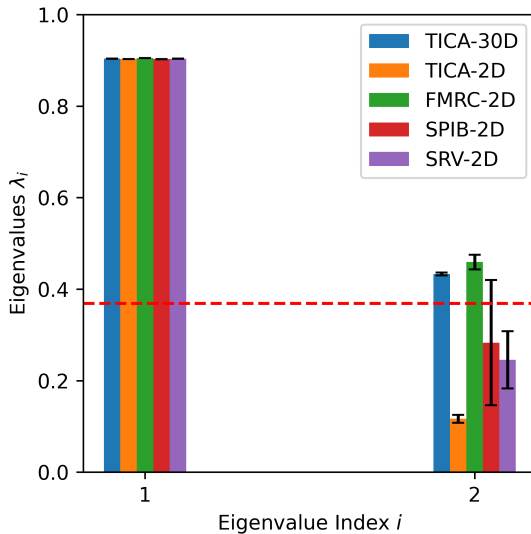


Figure 4: Comparison of $\hat{\lambda}_i^{MSM}$ of MSMs constructed in different RC spaces for CLN025. A red dashed line at $\lambda_i = 0.369$ indicates the cutoff for timescales shorter than the τ^{MSM} used for MSM construction, signifying that the constructed MSM has failed to identify this slow process.

for details) as our input features. We then selected a short lag time of $\tau = 2$ ns for RC learning. To establish an overview of the system, we performed a regular TICA+MSM analysis and identified two major slow processes in the system (Figure S1) at $\tau^{MSM} = 40$ ns. Our goal here is to construct an optimal RC that is sufficient to characterize the folding process and capture these two slow modes within its RC space.

Following the protocol described in Theory and Methods, we built a series of MSM by clustering inside Ψ_{TICA} spaces with different dimensions. We then selected the truncation dimension as $d_{int} = 30$ based on the comparison of $\hat{\lambda}_1^{MSM}$ and $\hat{\lambda}_2^{MSM}$ and used $[\hat{\psi}_1^{TICA}, \dots, \hat{\psi}_{30}^{TICA}]^\top$ as the input for our FMRC neural network. We then trained 10 FMRC models with the same hyperparameters (see Supporting Information) and obtained 10 \mathbf{r}^{FMRC} . For comparison, we learned both a 30-dimensional \mathbf{r}_{30D}^{TICA} and a 2-dimensional \mathbf{r}_{2D}^{TICA} . Although the algorithm is deterministic, we repeated the stochastic k-means clustering to obtain 10 MSMs for \mathbf{r}_{30D}^{TICA} and \mathbf{r}_{2D}^{TICA} to provide a reference to the variance introduced by k-means clustering. We also trained 10 SRV models using the input features directly and

the same hyperparameters (see Supporting Information). For SPIB, we performed k-means clustering inside the 30-dimensional Ψ_{TICA} space which we used as our FMRC input to generate the state labels $\mathbf{y}_{t+\tau}$. These state labels were then supplied to SPIB together with the input features as inputs. The training process was repeated 10 times with the same hyperparameters (See Supporting Information) for 10 SPIB models. We then calculated the mean and standard deviation of the MSM eigenvalues $\hat{\lambda}_i^{MSM}$ from these RC spaces for a quantitative comparison which we summarized the results in Figure 4.

From this eigenvalue comparison, we can see that there are no significant differences between the performance of capturing the slowest mode ψ_1 of the system. All models successfully encoded ψ_1 in their RC space with the correct timescale t_i and minimal variance. However, when it comes to ψ_2 , only \mathbf{r}^{FMRC} among the two-dimensional RCs consistently encodes this slow mode with minimal variance. In contrast, \mathbf{r}^{SPIB} , suffers from large modelling variance and can only capture this slow mode occasionally. Neither \mathbf{r}_{2D}^{TICA} nor \mathbf{r}^{SRV} is able to capture ψ_2 , underpinning the limitations of methods based on spectral decomposition. Notably, \mathbf{r}^{FMRC} outperforms even \mathbf{r}_{30D}^{TICA} , suggesting that \mathbf{r}^{FMRC} can efficiently encode a substantial amount of dynamical information in a reduced representation. This is consistent with the theoretical expectation that the lumpability and decomposability principles imply that the RC space spanned by $\mathbf{r}^{FMRC} \approx \mathbf{r}^{LD}$ has a reduced transfer operator $\mathcal{T}_{\mathbf{r}}(\tau)$ with leading eigenvalues similar to those of the original transfer operator $\mathcal{T}(\tau)$.

Next, we examine the minimum τ required for the ITS estimation to converge for MSMs constructed in different RC spaces. This property is practically important, since convergence with a shorter τ allows for shorter, parallel-sampled trajectories as input, which is known to enhance the sampling of transition events. Furthermore, MSMs constructed with shorter τ offer higher resolution and can provide more detailed biophysical insights. The ITS analysis in Figure S2 shows that MSMs constructed from \mathbf{r}^{FMRC} can consistently converge with a shorter τ . Moreover, MSM constructed from \mathbf{r}^{FMRC} can accurately predict future macrostate populations, as demonstrated by the Chapman-Kolmogorov test (Figure S3).

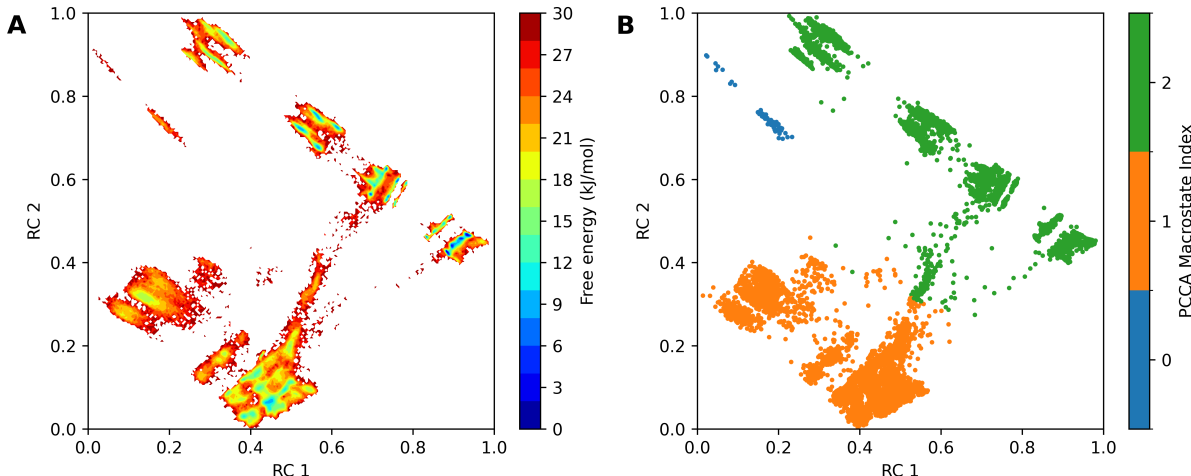


Figure 5: Free energy surface and macrostate assignment of CLN025. (A) The 2D FES projection of CLN025 and (B) the PCCA+ macrostate assignment projection for CLN025 in the normalized \mathbf{r}^{FMRC} space where the best MSM was constructed.

We then projected all data points \mathbf{x} of the trajectory to the 2D space defined by \mathbf{r}_{2D}^{TICA} , \mathbf{r}^{SRV} , \mathbf{r}^{FMRC} and \mathbf{r}^{SPIB} and calculated the 2D projected FES in these spaces (Figure 5A, S4A, S5A & S6A). Specifically, for \mathbf{r}^{SRV} , \mathbf{r}^{FMRC} and \mathbf{r}^{SPIB} , we utilized both the best and worst RC models for the projections to further examine variances arising from stochasticity. Notice there are at least 10 processes slower than the lag time τ used for RC learning, so a 2D FES projection in an RC space that sufficiently resolves all dynamics slower than τ should display at least 11 metastable basins separated by energy barriers. From these projections, we can see only \mathbf{r}^{FMRC} and \mathbf{r}^{SPIB} , which optimize RC using probabilistic modelling, meet this criterion. In contrast, \mathbf{r}_{2D}^{TICA} and \mathbf{r}^{SRV} fail to distinguish many actual metastable states in such low-dimensional representations. This outcome is reasonable and expected, since the approximated eigenfunctions from $\hat{\psi}_3^{TICA}$ or $\hat{\psi}_3^{SRV}$, which characterize transitions between these ignored metastable states, were truncated. These results highlight the significant pitfalls of using VAC-based \mathbf{r}^{TICA} or \mathbf{r}^{VAC} as RC, as discussed earlier in the Introduction section.

To further clarify the physical significance of the two slowest modes ψ_1 and ψ_2 , we use PCCA+³⁹ to group the microstates clustered in \mathbf{r}^{FMRC} space into three macrostates

(Figure 5B, S4B, S5B & S6B). The macrostates from PCCA+ are clustered in a way that microstates with similar $\hat{\psi}_i^{MSM}$ values are assigned to the same macrostate. This approach allows us to interpret the physical meaning of ψ_1 and ψ_2 by comparing the conformational ensembles of different PCCA+ macrostates. As shown in Figure S7, macrostate 1 represents the unfolded ensemble, while both macrostate 0 and macrostate 2 exhibit folded beta-hairpin structures with striking structural similarities. Upon close examination of their structural details (Figure S8), we found that all conformations in macrostate 0 have an inward-facing carbonyl oxygen on residue Glu5, whereas the same oxygen in macrostate 2 tends to face outward. Although macrostate 0 is indeed metastable, it is very rare, with a population of $\sim 0.2\%$ at equilibrium (Figure S7). In contrast, macrostate 2 is the true stable folded state, with a population of $\sim 78.2\%$ at equilibrium (Figure S7). Given that macrostate 0 is distant from the major folded state, we refer to it as a “misfolded” state. Despite its low population and striking structural similarity to the major folded state, correctly distinguishing this misfolded state from other metastable states is essential to correctly characterize the second slow mode of the system ψ_2 . To demonstrate this, we projected the PCCA+ assignments learned from the \mathbf{r}^{FMRC} space to one best and one worst RC space from each algorithm based on $\hat{\lambda}_i^{MSM}$ (Figure S4, S5 and S6). In general, MSMs with low $\hat{\lambda}_2^{MSM}$ values are built from RC spaces that cannot effectively distinguish this misfolded state. We further observed that while two-dimensional TICA and SRV struggle to differentiate this misfolded state, SPIB can occasionally do so. However, FMRC consistently differentiates this state, even in the worst-case scenario (Figure S9B).

Furthermore, by comparing FES projected on \mathbf{r}^{FMRC} and the PCCA+ macrostates assignment (Figure 5), we observed that the projection onto \mathbf{r}^{FMRC} reveals a highly detailed network structure within each macrostate, with smaller substates clearly delineated by small energy barriers. However, such a microscopic view may introduce redundant information and pose challenges for macroscopic interpretation from the projected FES. Beyond the PCCA+ clustering method, we found that tuning the learning lag time τ provides an alter-

native effective way to generate a macroscopic (or an even more microscopic) view (Figure S10 & S11). When training with different τ values, without altering other hyperparameters, FMRC consistently reveals more microscopic substates at shorter τ (Figure S10), while gradually merging them as τ increases (Figure S11). Notably, even as substrates merge, FMRC consistently distinguishes the sparsely populated misfolded state (Figure S11). As a result, the quality of the MSM constructed in these \mathbf{r}^{FMRC} spaces learned with different τ remains largely consistent across a range of τ (Figure S12), with the exception of very short τ , demonstrating the robustness of the FMRC algorithm in downstream analysis.

3.2 Complexity and Transition Networks: FMRC Analysis of Trp-Cage

We next proceeded to test FMRC on a more complex example: a 208 μs trajectory of the larger mini-protein Trp-Cage (DAYAQWLADGGPSSGRPPPS, 20 amino acids, PDB ID: 2JOF) folding simulated at 290K. We used a similar feature selection strategy to include extensive interatomic distances and dihedral angles as our input features. For this analysis, we used a slightly longer lag time of $\tau = 10$ ns compared to CLN025. As with the previous example, we initially conducted a regular TICA+MSM analysis to obtain an overall view of the system (Figure S13). The results suggest that, although Trp-Cage is only twice as long in sequence as CLN025, its transition network is significantly more complex, with a greater number of slow processes present in the system. As a result, at an MSM lag time $\tau_{MSM} = 50$ ns, there was no clear spectral gap among the top 20 eigenvalues. For this comparison between different RCs, we chose to focus on the top 11 slowest processes.

After testing for a range of d_{int} , we selected $d_{int} = 20$ as the truncation dimension for Ψ_{TICA} . The resulting $\Psi_{TICA} = [\hat{\psi}_1^{TICA}, \dots, \hat{\psi}_{20}^{TICA}]^T$ was used as the input for our FMRC neural network, following the exact same training protocol and hyperparameters as those used in the CLN025 example (see Supporting Information). Similarly, multiple models from repeated training were used to calculate mean and standard deviation of $\hat{\lambda}_i^{MSM}$ for the MSMs

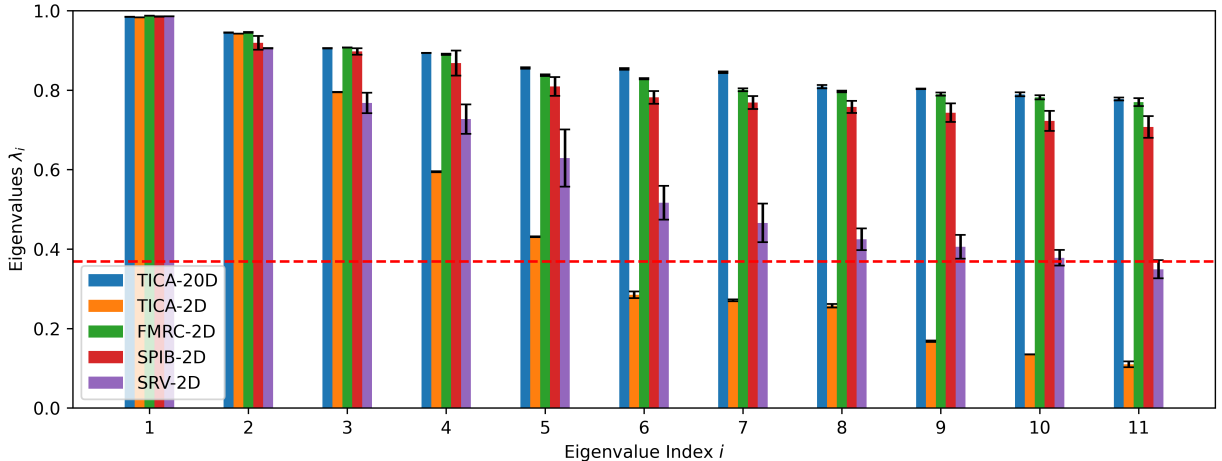


Figure 6: comparison of $\hat{\lambda}_i^{MSM}$ from MSMs constructed in different RC spaces for Trp-Cage. A red dashed line at $\lambda_i = 0.369$ marks the cutoff for timescales shorter than the τ^{MSM} used for MSM construction, indicating that the constructed MSM failed to capture this slow process.

built in each RC space spanned by \mathbf{r}_{20D}^{TICA} , \mathbf{r}_{2D}^{TICA} , \mathbf{r}^{SRV} , \mathbf{r}^{FMRC} or \mathbf{r}^{SPIB} (Figure 6).

Despite the increased complexity of the system, \mathbf{r}^{FMRC} consistently encodes a similar amount of the system’s major slow dynamics as a 20-dimensional \mathbf{r}_{20D}^{TICA} space, with minimal training variance, showing only a slight decay in the eigenvalues of the 5th to 9th MSM eigenvectors. In contrast, the VAC-based two-dimensional RCs \mathbf{r}_{2D}^{TICA} and \mathbf{r}^{SRV} exhibit a significant drop in performance starting from $\hat{\lambda}_3^{MSM}$. Specifically, \mathbf{r}_{2D}^{TICA} fails to identify the slow processes after $\hat{\psi}_5^{MSM}$. While introducing a neural network transformation to the input features significantly improves the performance of \mathbf{r}^{SRV} , the performances are still far from optimal, and the addition of the neural network introduces significant training variance.

On the other hand, \mathbf{r}^{SPIB} performs more satisfactorily, preserving the majority of the system dynamics. Yet, \mathbf{r}^{SPIB} is consistently outperformed by \mathbf{r}^{FMRC} in characterizing every slow mode, with greater training variance. These results are consistent with those observed in the CLN025 example, further underpinning the superior performance of \mathbf{r}^{FMRC} in encoding slow dynamics within its low-dimensional RC space.

As the system complexity increases, we observed that the ITS of MSM eigenvectors constructed in the \mathbf{r}^{FMRC} space does not always converge with the shortest τ (Figure S14).

Nevertheless, at $\tau_{MSM} = 50$ ns, as demonstrated by the Chapman-Kolmogorov test, the MSM constructed in \mathbf{r}^{FMRC} can provide very accurate predictions for almost all future macrostate populations (Figure S15).

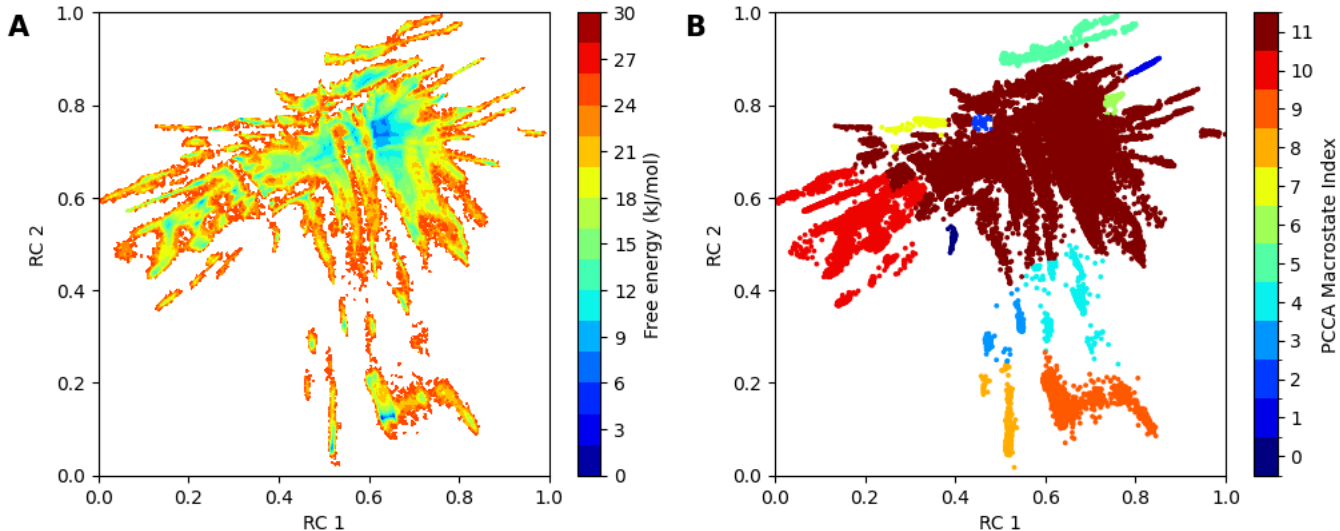


Figure 7: (A) The Trp-Cage 2D FES projection and (B) the Trp-Cage PCCA+ macrostate assignment projection on the normalized \mathbf{r}^{FMRC} space where the best MSM was constructed.

We next examined the 2D FES and PCCA+ assignments projections in these 2D RC spaces (Figure 7, Figure S16, Figure S17 & Figure S18). Given the smaller variances in $\hat{\lambda}_i^{MSM}$, we focused only on the projections in the best RC spaces with the highest $\hat{\lambda}_i^{MSM}$. Consistent with the observations in CLN025, the VAC-based \mathbf{r}_{2D}^{TICA} and \mathbf{r}^{SRV} display limited resolution between substates within the major metastable basins and are unable to distinguish several metastable states. In contrast, both \mathbf{r}^{SPIB} and \mathbf{r}^{FMRC} provide a more detailed description of the transition network. The PCCA+ projection on \mathbf{r}^{FMRC} reveals multiple folded and misfolded states interconnected with a major unfolded state. Specifically, the native nuclear magnetic resonance (NMR) structure belongs to the macrostate 9, which contains multiple deepest basins and corresponds to the folded state (Figure S20). \mathbf{r}^{FMRC} further distinguishes several structurally similar but less stable misfolded states, which are interconnected through the major unfolded state, macrostate 11 (Figure S19 & S20). Such metastable state assignment can be distinguished by \mathbf{r}^{SPIB} in a satisfactory way, although

there are still some overlappings (Figure S18). This overlap might explain why the $\hat{\lambda}_i^{MSM}$ values for the MSMs constructed from \mathbf{r}^{SPIB} are generally lower than those constructed from \mathbf{r}^{FMRC} .

Finally, \mathbf{r}^{FMRC} can be adjusted to provide either a more microscopic or macroscopic description within its RC space by tuning the training lag time τ (Figure S21 & S22). However, as the complexity of the system increases, we notice that the final quality of the constructed MSM becomes more sensitive to the choice of τ (Figure S23). In general, adjusting τ has a smaller impact on the quality of the leading eigenvectors. This suggests that the choice of τ for learning \mathbf{r}^{FMRC} should be done with greater care, particularly if PCCA+ is used to cluster a large number of macrostates for a more detailed microscopic interpretation of the system.

3.3 Challenging System Size: FMRC Performance on NTL-9 Folding Dynamics

For our final example, we used a 1.11 ms trajectory of NTL-9 (MKVIFLKDVKGMGKKGEIKN-VADGYANNFLFKQGLAIEA, 39 amino acids, PDB ID:2HBA) folding simulated at 355K. This system, with almost double the protein sequence size compared to Trp-Cage, presents a further challenge for our FMRC learning algorithm. To manage the increased system size, we reduced the input features by excluding all sidechain and backbone $N - O$ interatomic distances (see Supporting Information for details). Furthermore, we strided the trajectory at a frequency of 5 to fit the dataset into memory. We used a lag time of $\tau = 20$ ns for all model training. As with the previous example, we began with a TICA+MSM analysis to obtain an overall picture of the system (Figure S24). Similar to Trp-Cage, NTL-9 exhibited numerous slow processes. However, our analysis suggested that a longer lag time of $\tau^{MSM} = 300$ ns was necessary for MSM construction to ensure Markovianity for all MSMs constructed in different RC spaces. We found that only 8 processes were slower than τ^{MSM} , and there was no clear spectral gap among the first 8 eigenvalues (Figure S24). Therefore, we focused on

the top 5 slowest processes of the system for further analysis.

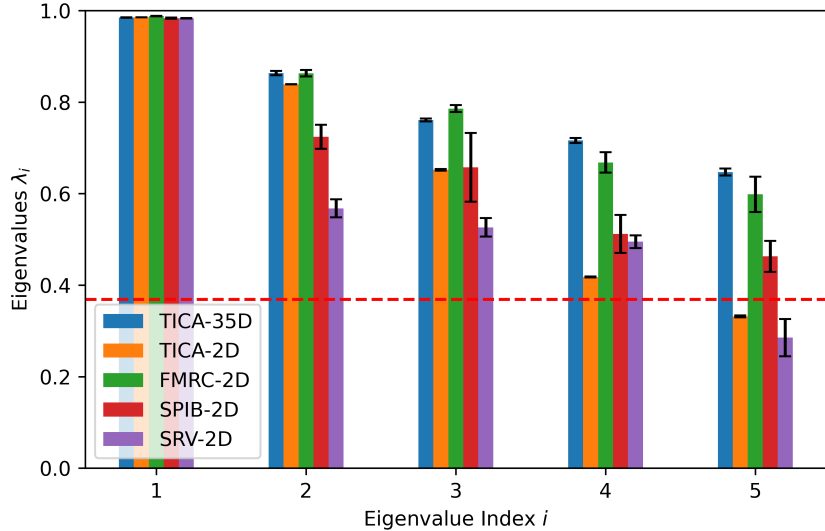


Figure 8: Comparison of $\hat{\lambda}_i^{MSM}$ of MSMs constructed in different RC spaces for NTL-9. A red dashed line at $\lambda_i = 0.369$ has been drawn to denote a cutoff for the corresponding timescales lower than the τ^{MSM} for MSM construction. This indicates that the constructed MSM has failed to identify this slow process.

We followed the same procedures as in CLN025 and Trp-Cage and selected $d_{int} = 35$. $\Psi_{TICA} = [\hat{\psi}_1^{TICA}, \dots, \hat{\psi}_{35}^{TICA}]^\top$ was then used as our FMRC neural network input and we used the same training hyperparameters as in CLN025 and Trp-Cage. Means and standard deviations were also obtained in similar procedures and the results are summarized in Figure 7. We can see that \mathbf{r}^{FMRC} similarly outperforms \mathbf{r}_{2D}^{TICA} , \mathbf{r}^{SRV} and \mathbf{r}^{SPIB} , while being able to match the performance of a 35-dimensional \mathbf{r}_{35D}^{TICA} . Specifically, \mathbf{r}^{FMRC} retains the system dynamics inside its RC space with only some slight decay in $\hat{\lambda}_4^{MSM}$ and $\hat{\lambda}_5^{MSM}$. MSM constructed in \mathbf{r}^{FMRC} also results in an improved estimation of $\hat{\psi}_3^{MSM}$ in comparison to the one constructed in \mathbf{r}_{35D}^{TICA} . In contrast, as the system complexity grows, the performance of \mathbf{r}_{2D}^{TICA} , \mathbf{r}^{SRV} and \mathbf{r}^{SPIB} significantly decay, and none of them are able to capture the slow processes ψ_5 in their low-dimensional RC spaces. In this particular example, only the MSM constructed in \mathbf{r}_{35D}^{TICA} converges with a shorter τ and the rest of MSMs do not have a significant difference in ITS convergence (Figure S25). Similarly, MSM constructed from

\mathbf{r}^{FMRC} can provide a sufficiently accurate prediction of the future macrostate population (Figure S26).

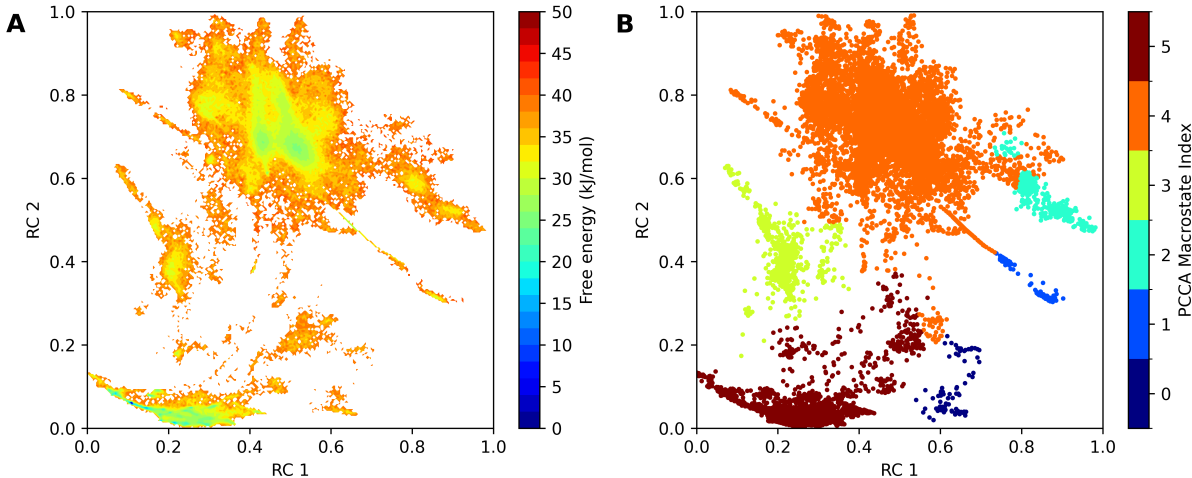


Figure 9: (A) The NTL-9 2D FES projection and (B) the NTL-9 PCCA+ macrostate assignment projection on the normalized \mathbf{r}^{FMRC} space where the best MSM was constructed.

We further projected 2D FES and PCCA+ assignments as in Trp-Cage using the best MSM constructed in different RC spaces (Figure 9, Figure S27, Figure S28 & Figure S29) and similar observations are also obtained. The 2D FES projection on \mathbf{r}^{FMRC} consists of numerous small basins divided by small energy barriers (Figure 9A). The PCCA+ assignment projection on \mathbf{r}^{FMRC} revealed a similar interconnected transition network between the major folded state (macrostate 5) and the major unfolded state (macrostate 4), accompanied by several less populated misfolded states, similar to the network structure in Trp-Cage. Representative conformations from each metastable state are presented in Figure S30. Similar trends follow that metastable states are all well distinguished in \mathbf{r}^{FMRC} and \mathbf{r}^{SPIB} (Figure S29, albeit to a lesser extent) and cannot be fully distinguished in VAC-based \mathbf{r}_{2D}^{TICA} or \mathbf{r}^{SRV} (Figure S27 & S28). By tuning τ , a more microscopic or more macroscopic representation by \mathbf{r}^{FMRC} can be similarly obtained (Figure S31 & S32). Interestingly, with the even more increased complexity, increasing τ for learning \mathbf{r}^{FMRC} actually further improves the quality of the constructed MSM (Figure S33), suggesting that the optimal choice of τ for learning \mathbf{r}^{FMRC} for MSM construction is very system specific and requires careful tuning.

4 Conclusion

Obtaining a low-dimensional RC representation of the system which effectively describes the full-dimensional dynamics of biomolecular MD trajectories is one of the key problems in the field of biomolecular simulations. Current methods, either require a supervised learning scheme (e.g. committor-based methods) that can potentially be misdirected by human inputs, or suffer from the linearity of the methods (VAC-based). In this article, we introduce a novel unsupervised RC machine learning algorithm, Flow Matching for Reaction Coordinates (FMRC), which is based on a novel definition of optimal RC of lumpability and decomposability from recent theoretical studies. The novel theoretical definition has a deep relationship with the well-established transfer operator theory and our re-formulation of their mathematical definitions into conditional probability enables the incorporation of such definition as an optimization target for deep learning. In contrast, this new formulation of optimal RC avoids the linearity problem presented in the VAC-based method and can be effectively learned through probabilistic modelling. Specifically, by representing the optimal RC as an encoder and using the FM architecture as decoders, we efficiently perform a search for the optimal \mathbf{r}^{FMRC} constructed from input features that satisfy lumpability and decomposability. We further demonstrate that \mathbf{r}^{FMRC} can effectively compress and incorporate a large amount of dynamic information in a two-dimensional space which can only be effectively described with a much higher dimensional \mathbf{r}^{TICA} coordinates for all three example systems with increased complexity. In contrast, neither VAC-based methods including TICA and SRV nor the information bottleneck based method SPIB can achieve such efficient system compression. Specifically, they all tend to have a significantly reduced performance when the system complexity increases whereas FMRC can perform consistently. Furthermore, FMRC also has a much smaller training variance and provides a much more consistent result. We also demonstrate that the training procedure is rather simple and a minimal number of hyperparameters require tuning.

Considering the importance of RC in simulation studies of biomolecules, we anticipate

the efficacy of the FMRC algorithm will make a difference in various downstream applications. Specifically, we would like to highlight their potential usage in MSM construction and collective variable (CV)-based enhanced sampling methods. For MSM construction, we demonstrate that FMRC can efficiently reduce the dimensions of the trajectory dataset and thus allow a faster clustering step at the cost of a slight decrease in MSM model quality in comparison to the conventional TICA dimension reduction. The resulting 2D projection inside the \mathbf{r}^{FMRC} space is also much richer in information in comparison to a \mathbf{r}_{2D}^{TICA} representation and much easier to interpret in comparison to a high-dimensional \mathbf{r}^{TICA} representation. Such 2D projection can serve as an effective complement to the visualization of the transition network between e.g. PCCA+ macrostates. Although we did not perform any kind of testing of \mathbf{r}^{FMRC} for CV-based enhanced sampling in this article, its ability to effectively encode large amounts of dynamics from data makes it a promising candidate method to alleviate the need for human expertise. However, there are two potential problems in such an application: 1) in this article, we assumed a data-rich scenario and did not investigate if an accurate \mathbf{r}^{FMRC} can be learned with limited initial sampling, although the theoretical studies on lumpability and decomposability suggest that \mathbf{r}^{FMRC} can be computed with sparse sampling.¹² 2) In our current study, we used hundreds to thousands of input features and computed the \mathbf{r}^{FMRC} with a relatively large neural network. As a result, the effective learning of \mathbf{r}^{FMRC} only requires limited human knowledge of the system as presented in this article. However, CV-based enhanced sampling methods often require iterative bias computation on-the-fly during the simulation and computing \mathbf{r}^{FMRC} can significantly slow down the simulation. We leave the investigation of the application of \mathbf{r}^{FMRC} and these considerations to future studies.

Acknowledgement

The authors thank D. E. Shaw research for providing the ultralong MD simulation trajectories used in this study. We acknowledge funding from the National Natural Science Foundation of China (1217011218 to H.W., 32371300 to Y.W.). Yong Wang acknowledges the financial support of the National Key Research and Development Program of China (No. 2021YFF1200404), and the Zhejiang Provincial National Science Foundation of China (No. LZ24C050003).

Supporting Information Available

Further details on the previously established theories and algorithms, including VAC, TICA, SRV, SPIB, and MSM construction, as well as additional figures supporting our results, can be found in the Supporting Information. This information is available free of charge via the Internet at <http://pubs.acs.org>.

References

- (1) Shaw, D. E.; Grossman, J.; Bank, J. A.; Batson, B.; Butts, J. A.; Chao, J. C.; Denneroff, M. M.; Dror, R. O.; Even, A.; Fenton, C. H.; et al., Anton 2: Raising the Bar for Performance and Programmability in a Special-Purpose Molecular Dynamics Supercomputer. SC '14: Proceedings of the International Conference for High Performance Computing, Networking, Storage and Analysis. 2014; pp 41–53.
- (2) Prinz, J.-H.; Wu, H.; Sarich, M.; Keller, B.; Senne, M.; Held, M.; Chodera, J. D.; Schütte, C.; Noé, F. Markov models of molecular kinetics: Generation and validation. *J. Chem. Phys.* **2011**, *134*.

- (3) Torrie, G. M.; Valleau, J. P. Nonphysical sampling distributions in Monte Carlo free-energy estimation: Umbrella sampling. *J. Comput. Phys.* **1977**, *23*, 187–199.
- (4) Laio, A.; Parrinello, M. Escaping free-energy minima. *Proc. Natl. Acad. Sci. USA* **2002**, *99*, 12562–12566.
- (5) Bussi, G.; Laio, A. Using metadynamics to explore complex free-energy landscapes. *Nat. Rev. Phys* **2020**, *2*, 200–212.
- (6) Wang, Y.; Ribeiro, J. M. L.; Tiwary, P. Past–future information bottleneck for sampling molecular reaction coordinate simultaneously with thermodynamics and kinetics. *Nat. Commun.* **2019**, *10*, 3573.
- (7) Chen, W.; Sidky, H.; Ferguson, A. L. Nonlinear discovery of slow molecular modes using state-free reversible VAMPnets. *J. Chem. Phys.* **2019**, *150*.
- (8) Pérez-Hernández, G.; Paul, F.; Giorgino, T.; De Fabritiis, G.; Noé, F. Identification of slow molecular order parameters for Markov model construction. *J. Chem. Phys.* **2013**, *139*.
- (9) McGibbon, R. T.; Husic, B. E.; Pande, V. S. Identification of simple reaction coordinates from complex dynamics. *J. Chem. Phys.* **2017**, *146*.
- (10) Kang, P.; Trizio, E.; Parrinello, M. Computing the committor with the committor to study the transition state ensemble. *Nat. Comput. Sci.* **2024**, 1–10.
- (11) Lazzeri, G.; Jung, H.; Bolhuis, P. G.; Covino, R. Molecular free energies, rates, and mechanisms from data-efficient path sampling simulations. *J. Chem. Theory Comput.* **2023**, *19*, 9060–9076.
- (12) Bittracher, A.; Mollenhauer, M.; Koltai, P.; Schütte, C. Optimal reaction coordinates: Variational characterization and sparse computation. *Multiscale Model. Simul.* **2023**, *21*, 449–488.

- (13) Onsager, L. Initial recombination of ions. *Phys. Rev.* **1938**, *54*, 554.
- (14) Du, R.; Pande, V. S.; Grosberg, A. Y.; Tanaka, T.; Shakhnovich, E. S. On the transition coordinate for protein folding. *J. Chem. Phys.* **1998**, *108*, 334–350.
- (15) Jung, H.; Covino, R.; Arjun, A.; Leitold, C.; Dellago, C.; Bolhuis, P. G.; Hummer, G. Machine-guided path sampling to discover mechanisms of molecular self-organization. *Nat. Comput. Sci.* **2023**, *3*, 334–345.
- (16) Noé, F.; Nüske, F. A variational approach to modeling slow processes in stochastic dynamical systems. *Multiscale Model. Simul.* **2013**, *11*, 635–655.
- (17) Wu, H.; Noé, F. Variational approach for learning Markov processes from time series data. *J. Nonlinear Sci.* **2020**, *30*, 23–66.
- (18) Wu, H.; Nüske, F.; Paul, F.; Klus, S.; Koltai, P.; Noé, F. Variational Koopman models: Slow collective variables and molecular kinetics from short off-equilibrium simulations. *J. Chem. Phys.* **2017**, *146*.
- (19) Schwantes, C. R.; Pande, V. S. Modeling molecular kinetics with tICA and the kernel trick. *J. Chem. Theory Comput.* **2015**, *11*, 600–608.
- (20) McKiernan, K. A.; Husic, B. E.; Pande, V. S. Modeling the mechanism of CLN025 beta-hairpin formation. *J. Chem. Phys.* **2017**, *147*.
- (21) Sidky, H.; Chen, W.; Ferguson, A. L. High-resolution Markov state models for the dynamics of Trp-cage miniprotein constructed over slow folding modes identified by state-free reversible VAMPnets. *J. Phys. Chem. B* **2019**, *123*, 7999–8009.
- (22) Bonati, L.; Piccini, G.; Parrinello, M. Deep learning the slow modes for rare events sampling. *Proc. Natl. Acad. Sci. USA* **2021**, *118*, e2113533118.

- (23) Plattner, N.; Doerr, S.; De Fabritiis, G.; Noé, F. Complete protein–protein association kinetics in atomic detail revealed by molecular dynamics simulations and Markov modelling. *Nat. Chem.* **2017**, *9*, 1005–1011.
- (24) Plattner, N.; Noé, F. Protein conformational plasticity and complex ligand-binding kinetics explored by atomistic simulations and Markov models. *Nature communications* **2015**, *6*, 7653.
- (25) Brotzakis, Z. F.; Limongelli, V.; Parrinello, M. Accelerating the calculation of protein–ligand binding free energy and residence times using dynamically optimized collective variables. *J. Chem. Theory Comput.* **2018**, *15*, 743–750.
- (26) Bittracher, A.; Banisch, R.; Schütte, C. Data-driven computation of molecular reaction coordinates. *J. Chem. Phys.* **2018**, *149*.
- (27) Bittracher, A.; Koltai, P.; Klus, S.; Banisch, R.; Dellnitz, M.; Schütte, C. Transition manifolds of complex metastable systems: Theory and data-driven computation of effective dynamics. *J. Nonlinear Sci.* **2018**, *28*, 471–512.
- (28) Tishby, N.; Pereira, F. C.; Bialek, W. The information bottleneck method. *arXiv preprint physics/0004057* **2000**,
- (29) Wang, D.; Tiwary, P. State predictive information bottleneck. *J. Chem. Phys.* **2021**, *154*.
- (30) Mehdi, S.; Wang, D.; Pant, S.; Tiwary, P. Accelerating all-atom simulations and gaining mechanistic understanding of biophysical systems through state predictive information bottleneck. *J. Chem. Theory Comput.* **2022**, *18*, 3231–3238.
- (31) Wang, D.; Qiu, Y.; Beyerle, E. R.; Huang, X.; Tiwary, P. Information Bottleneck Approach for Markov Model Construction. *J. Chem. Theory Comput.* **2024**,

- (32) Wang, D.; Tiwary, P. Augmenting Human Expertise in Weighted Ensemble Simulations through Deep Learning based Information Bottleneck. *arXiv preprint arXiv:2406.14839* **2024**,
- (33) Zhang, Z.; Guo, L.; Wu, H. Flow Matching Approach to Reaction Coordinate Evaluation and Optimization. *arXiv preprint arXiv:2408.15981* **2024**,
- (34) Chen, R. T.; Rubanova, Y.; Bettencourt, J.; Duvenaud, D. K. Neural ordinary differential equations. *Adv Neural Inf Process Syst* **2018**, *31*.
- (35) Lipman, Y.; Chen, R. T.; Ben-Hamu, H.; Nickel, M.; Le, M. Flow matching for generative modeling. *arXiv preprint arXiv:2210.02747* **2022**,
- (36) Tong, A.; Malkin, N.; Huguet, G.; Zhang, Y.; Rector-Brooks, J.; Fatras, K.; Wolf, G.; Bengio, Y. Improving and generalizing flow-based generative models with minibatch optimal transport. *arXiv preprint arXiv:2302.00482* **2023**,
- (37) Lindorff-Larsen, K.; Piana, S.; Dror, R. O.; Shaw, D. E. How fast-folding proteins fold. *Science* **2011**, *334*, 517–520.
- (38) Noé, F.; Clementi, C. Kinetic distance and kinetic maps from molecular dynamics simulation. *J. Chem. Theory Comput.* **2015**, *11*, 5002–5011.
- (39) Röblitz, S.; Weber, M. Fuzzy spectral clustering by PCCA+: application to Markov state models and data classification. *Adv. Data Anal. Classif.* **2013**, *7*, 147–179.
- (40) Hoffmann, M.; Scherer, M. K.; Hempel, T.; Mardt, A.; de Silva, B.; Husic, B. E.; Klus, S.; Wu, H.; Kutz, J. N.; Brunton, S.; Noé, F. Deeptime: a Python library for machine learning dynamical models from time series data. *Mach. learn.: sci. technol.* **2021**,

TOC Graphic

